Materials and Design 155 (2018) 46–58

Contents lists available at ScienceDirect

Materials and Design

journal homepage: www.elsevier.com/locate/matdes

Design and fabrication of melt electrowritten tubes using intuitive software

Erin McColl [a,b], Jürgen Groll [a], Tomasz Jungst [a,*], Paul D. Dalton [a,*]

[a] Department for Functional Materials in Medicine and Dentistry and Bavarian Polymer Institute, University of Würzburg, Pleicherwall 2, 97070 Würzburg, Germany
[b] Institute of Health and Biomedical Innovation, Queensland University of Technology, 60 Musk Avenue, Kelvin Grove 4059, Australia

HIGHLIGHTS

- A web-based application with intuitive controls allows the design of different tubes, and automatically generates G-codes.
- A continuous direct-writing path around a cylinder was calculated and tested with a melt electrowriting printer.
- Melt electrowritten tubes had the winding angle, number of pivot points and pore size match predictions.

GRAPHICAL ABSTRACT

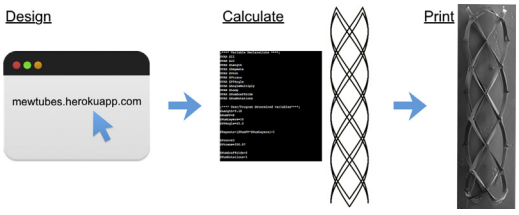

ARTICLE INFO

Article history:
Received 21 March 2018
Received in revised form 16 May 2018
Accepted 16 May 2018
Available online 21 May 2018

Keywords:
Additive manufacturing
3D printing
Electrohydrodynamic printing
Biomaterials
Polycaprolactone

ABSTRACT

This study approaches the accurate continuous direct-writing onto a cylindrical collector from a mathematical perspective, taking into account the winding angle, cylinder diameter and length required for the final 3D printed tube. Using an additive manufacturing process termed melt electrowriting (MEW), porous tubes intended for tissue engineering applications are fabricated from medical-grade poly(ε-caprolactone) (PCL), validating the mathematically-derived method. For the fabricated tubes in this study, the pore size, winding angle and printed length can all be planned in advance and manufactured as designed. The physical dimensions of the tubes matched theoretical predictions and mechanical testing performed demonstrated that variations in the tubular morphology have a direct impact on their strength. MEWTubes, the web-based application developed and described here, is a particularly useful tool for planning the complex continuous direct writing path required for MEW onto a rotating, cylindrical build surface.

1. Introduction

Additive manufacturing (AM) has become adopted within numerous disciplines, including aerospace, automotive, textiles and biomedical engineering [1–3]. Every AM technique has its pros and cons from the manufacturing context, and includes technologies such as fused deposition modeling, dispense plotting, stereolithography, electron beam melting and selective laser sintering [2]. There are other, less researched, AM approaches that include mosaic hydrogels [4], robocasting [5], laser-assisted free-form writing [6], magnetic 3D bioprinting [7] and the AM technology described here, melt electrowriting (MEW) [8]. The capabilities of these emerging AM technologies remain to be fully investigated, while their efficacy of use in certain applications is still being ascertained.

MEW is a nozzle-based AM technology that continuously direct-writes with electrohydrodynamically stabilized molten polymer jets [8]. Upon contact with a collector, the molten jet rapidly solidifies into a defined fiber, that can be layered using direct-writing principles.

* Corresponding authors.
E-mail addresses: tomasz.juengst@fmz.uni-wuerzburg.de, (T. Jungst), paul.dalton@fmz.uni-wuerzburg.de (P.D. Dalton).

https://doi.org/10.1016/j.matdes.2018.05.036

There are both printer and material properties that influence the deposited fiber, and can be modelled [9,10]. One important aspect of MEW is the dimensional spectrum of fibers that can be direct-written in a single print (5 to 50 μm), through the combination of air pressure and collector speed and the control of their placement [10].

The implications of this smaller diameter filament are particularly pertinent to applications in the biomedical sciences, where cells and organized tissues are of similar scale to the MEW filaments. Furthermore, constructs made via MEW typically have a high porosity, over 90% [11], and have been applied to cancer research [12], implantable devices [13] and tissue engineering [14]. The surfaces can be chemically modified with known processes [12,15], and the mechanical properties of such scaffolds are notably strengthened – up to 54-fold – when combined with a hydrogel matrix [11,16,17]. Importantly, the positioning accuracy of the fibers was shown to be essential for the significant improvements in mechanical properties [18].

From a direct-writing perspective, MEW has two specific limitations that are both relevant to this study. Firstly, rapid "on-off" printing with the electrified, viscoelastic jet is not readily achieved, so the printed material requires fabrication from a continuous single fiber deposited onto the build-plate/collector. The second limitation is the lag induced between the nozzle and the collector surface due to any disparity between the polymer ejection velocity and the rate of print head movement (Fig. 1a) [19].

While the majority of MEW research to date has been performed on flat collectors, cylindrical mandrels have also been used as a collector surface [20,21]. In these previous studies a free spinning mandrel approach has been adopted, similar to mechanically winding fibers to produce a tubular construct [22]. To move beyond the current free spinning mandrel approach for MEW, here we used a more controlled mandrel movement in conjunction with fiber path planning to achieve a work/flow for the AM of tubular structures that includes an online programming tool. Therefore, this paper looks at creating a precisely controlled direct-writing method which harnesses software written to enable AM of tubular scaffolds without a user needing to be aware of the underlying mathematics or machine code. This method of AM and the designed software were verified by printing tubes and comparing them to the theoretical model to determine accuracy and reproducibility.

2. Materials and methods

2.1. Melt electrowriting (MEW)

Poly(caprolactone) (PCL) was sourced from PURAC (PC-12; lot# 1412000249, 03/2015, Gorinchem, Netherlands), and used after storage as previously described [19]. A custom-built MEW machine was used in standard room temperature conditions in the range of 20–22 °C and a relative humidity of 30–45%. The printer has a rotating mandrel mounted on a x- and y-axis (Aerotech, Pittsburgh USA), and a custom print head affixed to a z-axis (Aerotech, Pittsburgh USA). The configuration is depicted in Fig. 1a which shows an electrified jet being drawn towards the grounded mandrel. The mandrel is coupled to a DC motor with an encoder attached to enable precise digital tracking of the mandrel's speed and position (0.36° ± 0.18°). The diameter of the mandrel, a metal rod, is 1.5 mm for all experiments. Additionally, there is a small 2 × 7 cm rectangular collector nearby that is used to direct-write upon, to stabilize the electrified jet prior to printing. The other components of the tubular printer include a high voltage device (Spraybase, Ireland) which also provided air pressure to a 3 mL syringe, with a 22-gauge needle. The polymer was heated to a molten state using a custom electrical heater (JUMO, Germany). The voltage, pressure, temperature and collector distance were maintained at fixed values of 7 kV, 1 bar, 89 °C and 4 mm respectively, throughout.

2.2. Web-based application for tube design

An open-access web-based application called "MEWTubes", was written to take user defined tube parameters and determine the machine control parameters (axes and mandrel velocity vectors) required to create specific structures on the MEW printer described. The web-based application is an implementation of the mathematical relationships required to translate user's tube requirements into machine code as well as presenting users with a visual digital representation of the designed tubular frame. This programme is capable of outputting the required machine code (for the MEW printer described) so that users require no programming knowledge. The machine used in this study uses a proprietary Aerotech programming environment

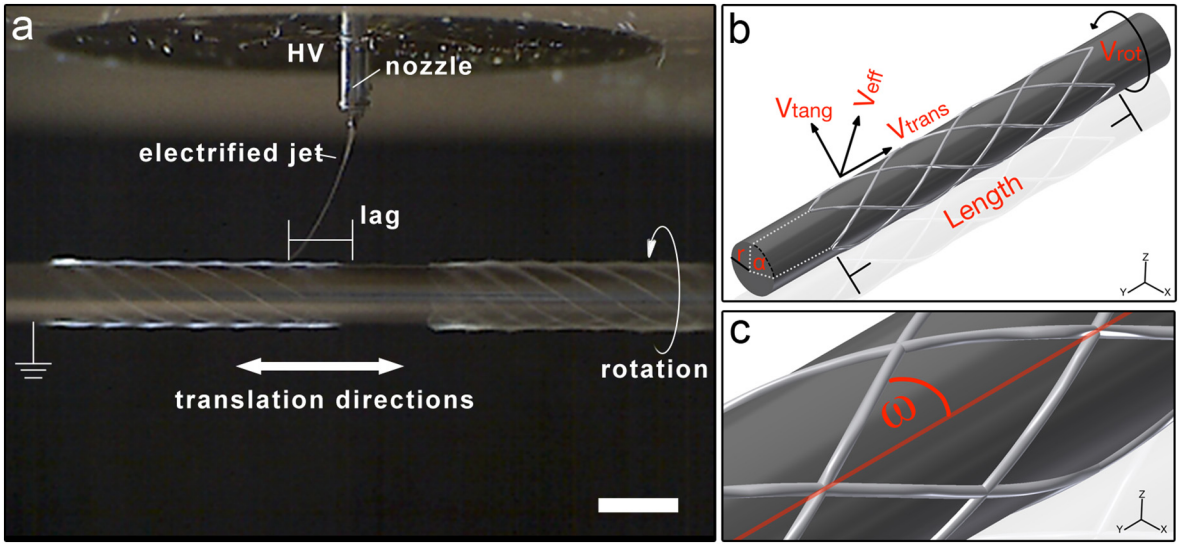

Fig. 1. a) Photograph of the MEW configuration, showing the nozzle where the high voltage (HV) is applied and the rotating, grounded mandrel, which also translates as it is rotated. There is typically a lag when the rotation/translation is faster than the speed of the electrified molten jet. Scale bar is 2 mm. The possible mandrel velocities; Translational (V_{trans}), tangential (V_{tang}), rotational (V_{rot}) and effective (V_{eff}) are shown in b) as well as the tube length, radius (r) and the pivot angle (α) between pivot points. While c) depicts how the winding angle (ω) is measured for a fiber placed on the mandrel.

(AeroTech Motion Composer Suite) which uses a variation of G-code that includes programmatic control flow constructs.

The source code for the MEWTubes application used here can be accessed from an open source repository (https://github.com/erinmccoll/MewTubes) and is hosted online for simplified access http://mewtubes.herokuapp.com. The back-end is written in Python taking advantage of the numpy and flask libraries, while the front end uses a combination of the bootstrap and VisJs packages along with custom HTML/JS/CSS as per standard web development.

2.3. Mathematical relationships required for successful tube fabrication

To design, simulate and create a tube with precisely controlled parameters, there exists some basic mathematics defining the relationship between these parameters and machine operation. The machine parameters include the rotational velocity of the mandrel (V_{rot}) in revolutions/minute (rpm), translational velocity (V_{trans}) in mm/min and the radius of the mandrel (r). Scaffold design parameters include the length (L) and winding angle (ω). These parameters are depicted graphically in Fig. 1b and are all inputs into the web-based application. In order to manufacture tubes with predictable dimensions and mechanical properties, it is necessary to explore and understand these relationships.

The **winding angle** is the angle made between the placed fiber and a central line running along the axial length of the mandrel (Fig. 1c). The combination of rotational and translational speed of the mandrel defines how tightly the fiber is wrapped around the mandrel. Eq. (1.1) defines this behavior mathematically, where the winding angle (ω) is determined by the ratio of the tangential velocity (V_{tang}) and translational velocity (V_{trans}) for any winding angle from 0° to 90°. The tangential velocity (calculated as mm/min) is the rotational velocity of the mandrel (rpm) multiplied by the mandrel radius; a measure of the velocity on the surface of the mandrel, Eq. (1.2) shows this mathematically. Using Eqs. (1.1) and (1.2), combinations of V_{rot} and V_{trans} can be determined for a given winding angle. Although only the V_{rot} and V_{trans} variables are required as inputs to the machine code, it is important to calculate the effective velocity (V_{eff}) to ensure experimental consistency. The combined speeds of the axes can influence the pulling of fiber which in turn can affect fiber diameter. Effective velocity is the resultant velocity of the translational and tangential velocities as shown in Eq. (1.3).

$$\omega = ArcTan\left(\frac{V_{tang}}{V_{trans}}\right) \tag{1.1}$$

$$V_{tang} = r(V_{rot} \cdot 2\pi) \tag{1.2}$$

$$V_{eff} = \sqrt{{V_{trans}}^2 + {V_{tang}}^2} \tag{1.3}$$

For a given mandrel radius/tube size there exist many possible rotational and translational velocity combinations which will achieve the required winding angle. However, each combination will result in a different effective velocity and in practice some effective velocities work better than others. For a linearly placed fiber it is important, however, that the effective velocity is greater than the speed of the electrified polymer jet [19]. Increasing the effective velocity further will increase the polymer jet lag. Within the web-based application, a table is presented showing many possible rotational/translational combinations and their associated effective velocity. While the chosen effective velocity does not theoretically change the tubular scaffold, it does affect the stability of the jet and printing process. Selection of an effective velocity is at user discretion and will require trial and error on the given machine with the given parameters (temperature, pressure, voltage, printing distance, nozzle diameter). Within this study the velocity combinations were chosen to ensure that the effective velocity remains as close to 506 mm/min as possible.

The second important mathematical relationship is between the **length** of a tube and the fiber placement. The length (which is a user-defined variable) determines when the change in direction of the Y-axis translation should occur. These locations, where one length iteration ends and the next begins, have been designated **pivot points**. The controlled mandrel method employed by this study is dependent on knowing the precise position of these pivot points. As seen in Fig. 1b these pivot points are distributed around the circumference of the mandrel. When the number of pivot points is known, the number of degrees between each pivot point - termed the pivot angle (α) - can be calculated and used to position the mandrel precisely at the start of each length iteration.

The combination of V_{rot} and V_{trans} creates a helical curve around the mandrel. The location that the translation direction changes within the resulting curve affects where the pivot points are positioned at the end of a length cycle. To achieve a repetitive, defined structure with stacked fiber walls, the location of these pivot points must be known and controlled. If a user defines a random length value, there is no control over the pivot point location or guarantee that the helical pattern will sync up to enable correctly stacked layers. Fig. 2 displays this graphically in three dimensions, where two conditions are shown. In Fig. 2b, a random length was chosen (tube length = 3.25 mm), whereas the length value in Fig. 2a was determined based on the number of pivot points, in this case 4 pivot points (tube length = 3.24 mm). The length iterations (L1, L2, L3 and L4) are all equal and correspond to the chosen length value (3.25 mm or 3.24 mm).

Fig. 2-A2 shows that after the fourth length iteration a full helical revolution is completed and the end of the fourth iteration joins back up with the initial point, thereby completing each of the pivot point pairs and the first layer of fibers. All proceeding layers follow the same pattern, completing enough length cycles to reach the initial point again as demonstrated in Fig. 2-A4. Whereas, if a random length value is chosen, for example 3.25 mm (Fig. 2-B1) a single revolution of the helical curve is not divided by a known value. After four length iterations (Fig. 2-B2, B3) the final iteration does not meet back up with the original position. By continuing the pattern set by this length (Fig. 2-B4, B5), this misalignment continues and will do so for further length iterations. Given that the pivot angle is unknown, the mandrel control method cannot be implemented and repeated fiber placement cannot be achieved.

To enable mandrel control that results in controlled stacking, a length–pivot point relationship was mathematically defined and incorporated into a web-based application. The pitch length (λ) of the helix must first be determined as shown in Eqs. (2.1), where r is the radius and ω is the winding angle.

$$\lambda = \frac{2\pi r}{tan\,(\omega)} \tag{2.1}$$

Given the pitch length (λ), a fraction multiplier (F_m) variable can be used to determine how much of a full helical revolution is completed in a single length of the print. This is assuming that a single revolution or, helical pitch is used, however, a fraction of multiple revolutions (R_m) could also be considered. Therefore, the combined value of the fraction multiplier and the revolution multiplier is multiplied by the pitch length to determine a tube length. Eq. (3.1) shows how these variables and pitch length relate to define a length value.

$$L = \lambda(F_m + R_m) \tag{3.1}$$

In Fig. 2b the fraction multiplier is uncontrolled and is forced by the randomly chosen length value. For the case of Fig. 2a the fraction multiplier is precisely controlled at 0.25 and the length is subsequently output to be 3.24 mm. The ratio of the fraction multiplier and pitch length determines how many length iterations (L_i) are required until the fiber pairs are completed and the second layer can begin. For example, a fraction multiplier of 1 would result in a complete revolution in a

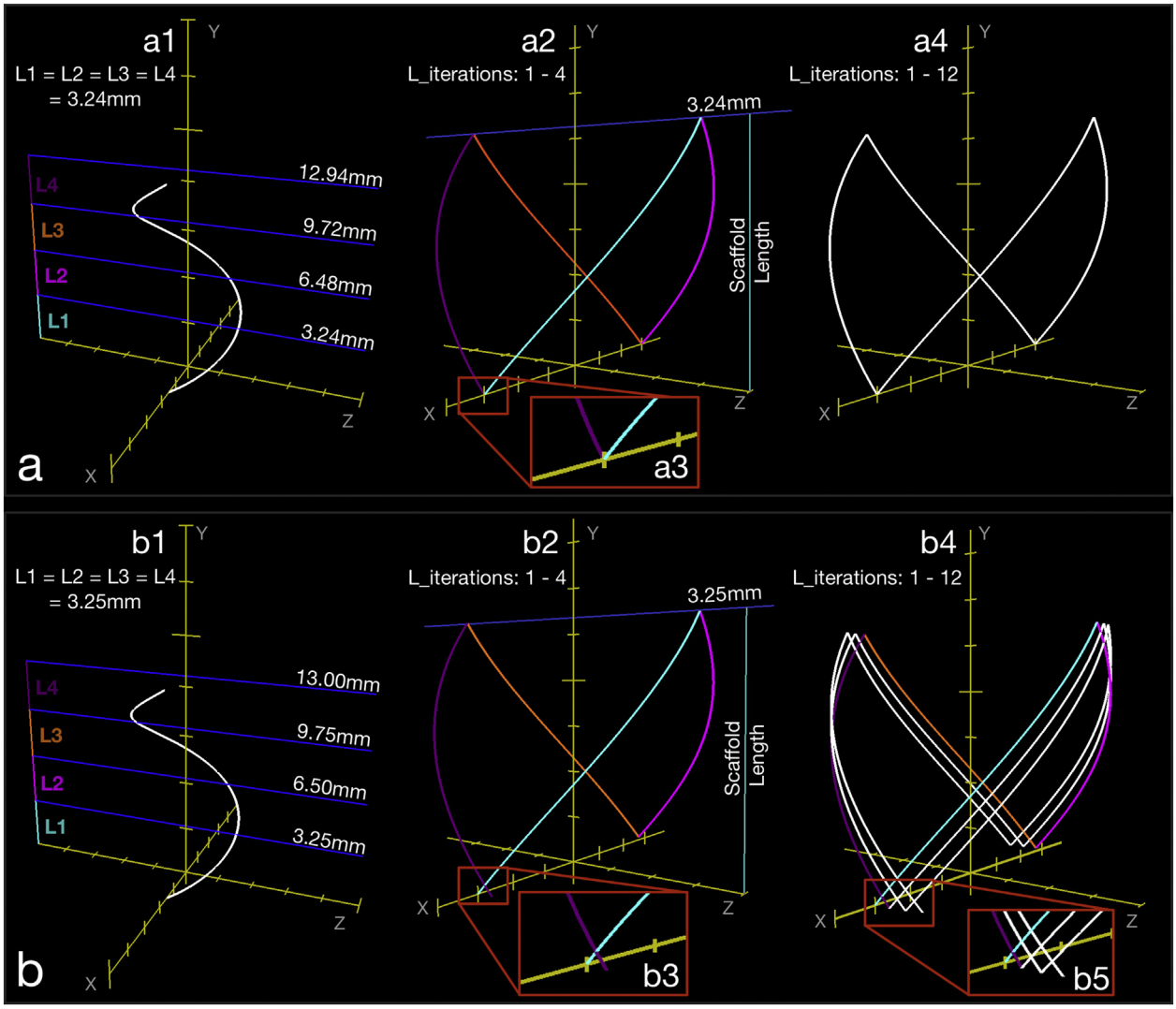

Fig. 2. An illustration of the 3D mathematical model for the fiber path of a tube with a 20° winding angle and 1.5 mm inner diameter. (a) Shows this model when a known fraction multiplier of 0.25 is used to achieve a scaffold length of 3.24 mm (Eq. (3.1)). (b) Depicts an example when a random length value (3.25 mm) is chosen forcing an unknown fraction multiplier. (A1 & B1) Show how a single helical revolution is divided depending on the scaffold length. While (A2, and B2) show the fiber path after 4 length iterations. A3, clearly shows that the 1st and 4th length iteration meets back up, while B3 shows that this is not achieved for a length of 3.25 mm. These models are extended further to 12 length iterations (A4, B4). While A4 is a controlled repetitive structure with each length iteration overlapping appropriately, B5 shows a close up of the continued uncontrolled fiber placement.

single length iteration (L_1), whereas a fraction multiplier of 0.25 (one quarter) requires four length iterations (L_4) for synchronization to occur - at which point there would be four pivot points (two at each end). These examples assume that a fraction of a single revolution occurs in one length iteration ($R_m = 0$), however two, three or four revolutions plus the fraction multiplier ($F_m + R_m$) could also be planned within a single tube length. This means that for a fixed pitch length (fixed winding angle and radius), there exists an array of valid lengths available. The fraction multiplier (F_m) is calculated in Eq. (4.1) where η is a whole number divisor of 360°. Given that a tube must have an even number of pivot points to complete the pairs in a single layer, the number of pivot points (N) can be η if it is even, or 2η if it is odd Eq. (4.2). The number of pivot points is then used to define the pivot angle (α), the rotation angle of the mandrel between each pivot point, as shown in Eq. (4.3). (The relationship between the number of pivot points, fraction multiplier and pivot angle is tabulated and explained further in a later section).

$$F_m = \frac{1}{\eta} \tag{4.1}$$

$$N = \eta + (\eta \ (\eta \ mod \ 2)) \tag{4.2}$$

$$\alpha = \frac{360^\circ}{N} \tag{4.3}$$

Overall, while the length is a user defined variable, it is essential that this length value should be chosen with a fixed fraction multiplier to guarantee a known pivot angle and ensure that the helical path is controlled and repeatable.

2.4. Imaging

A Zeiss steREO Discovery V2.0 microscope (Carl Zeiss, Oberkochen, Germany) was used to image and measure each sample. The **tube lengths** were measured using the Zeiss software caliper tool (Zeiss Zen Blue). This tool was placed to measure where the bulk of fibers ended, five measurements were taken for each of the three samples printed (n = 15) for each tested condition, the average was calculated with the error bars showing the standard deviation.

The **winding angle** of fibers was measured using the angle tool in the Zeiss software. Intersections were imaged from directly above and the angle measured along the top fiber in the stack, from the centerline of one fiber to the centerline of the next. Ten angles were randomly selected and measured for each of three printed samples (n = 30) in each tested condition.

The optical microscope was also used to **measure pore size** using the Zeiss software polygon tool. This tool was used to mark an area within the stacked fiber walls using the base fiber (the first layer) as the outline reference. While this measurement does not account for the curvature of the mandrel, it can compare the pore size variation between samples of the same collector diameter. One limitation of this approach is that the larger the pore size (i.e. the further it warped around the curved surface), the larger the error for such measurements.

A scanning electron microscope (SEM), specifically a Crossbeam 340 SEM (Carl Zeiss Microscopy, Gottingen, Germany) equipped with a Zeiss Gemini column, was used for high precision qualitative imaging. Samples were coated with platinum using a Leica EM ACE600 high vacuum sputter coater.

2.5. Theoretical pore size

A theoretical pore size was calculated and used to compare against the measured pore size to determine the print accuracy. The theoretical pore size can be determined for a scaffold given radius, winding angle and pivot angle. The diamond-shaped pores are wrapped three-dimensionally around the mandrel. However, the area of the pore can still be calculated using the arc length (L_A) as the distance between the two corners perpendicular to the tube length (Supplementary Fig. S1). This distance is the same as calculating the circumferential distance between two pivot points at the end of a tube. Eq. (5.1) details the formulation of the arc length, which is then used to determine the height of the equilateral triangle (H_T) in Eq. (5.2). Given these two values, the total area of the pore can be found as per Eq. (5.3).

$$L_A = 2\pi r\left(\frac{2\alpha}{360}\right) \tag{5.1}$$

$$H_T = \frac{0.5 \cdot L_A}{\tan(\omega)} \tag{5.2}$$

$$PoreArea = H_T \cdot L_A \tag{5.3}$$

2.6. Mechanical testing

An ElectroForce 5500 micro mechanical tester (Bose, Germany) was used for the mechanical testing in conjunction with a 250 g Honeywell load cell and the accompanying WinTest7 software. Three sample sets (Table 1) were tested under a tangential compressive force. Unmodified tubes were placed horizontally on a flat plate so that a compressing axis was applied tangentially to the major axis of the tube. A 20% compressive force was applied to all samples at a constant rate of 0.1 mm/s, with 20 readings/s being saved.

The first of the three sample sets considered a 45° winding angle with 10-layers (Group 1). Samples within this set were varied to have a different number of pivot points and subsequently varying pore sizes. Pivot points of 12, 14, 16 and 18 were tested. The second dataset (Group 2) also considered a 45° winding angle and varied the number of pivot points (12, 14, 16, 18), however the number of layers was adjusted for each condition so that the total volume of fiber stayed consistent. To verify this an electronic balance (Sartorius MC, Germany) was used to measure the sample weights. The weight was averaged across the six samples (n = 6) used per condition e.g. 12, 14, 16 and 18 pivot points. To account for the slight variation in sample lengths, as required to achieve the correct winding angle, a weight/length ratio was calculated and used for comparison.

Table 1
Tubes produced for mechanical testing. Group 1 and Group 2, both had winding angles of 45° and contained samples with 12, 14, 16 and 18 pivot points and were varied only by the number of length iterations used. Group 1 ensured enough iteration to achieve 10-layers while Group 2 had a fixed number of 80 length iterations - a value used to ensure that approximately the same volume of fiber was used across all samples. Group 3 included a range of winding angles each with a chosen pivot point value to ensure the pore size remained approximately 0.4 mm^2. Additionally, the number of length repeats for Group 3 was held constant at 80.

Sample set	Winding angle	Number of layers	Number of length iterations	Number of pivot points
Group 1	45°	10	varied	12 14 16 18
Group 2		varied	80	
Group 3	20°	~5	80	16
	30°	~6		14
	45°	~8		10
	60°	10		8
	70°	~14		6

The final sample set (Group 3) consisted of tubes with varying winding angles; 20°, 30°, 45°, 60° and 70°. In an attempt to keep these samples as consistent as possible, the pore size and number of layers were controlled. Based on previously measured pore size data, a pivot point condition was selected for each winding angle that resulted in a pore size of ~0.4 mm^2; 16-pivot points for 20°, 14 for 30°, 10 for 45°, 8 for 60° and 6 for 70°. For each condition within these three sample sets, six instances (n = 6) were printed, weighed and tested.

A three-point bending experiment was also performed with Group 3. The tubes were mounted horizontally as simply supported members with supports 6 mm apart. The bending properties were observed and photographed for qualitative analysis. A single tube from each condition in the Group 3 sample set was filmed and photographed undergoing three-point bending (Supplementary Fig. S2 & Supplementary Videos 1–5).

3. Results and discussion

While previous studies have fabricated MEW tubes with controlled winding angles, the fiber placement, spacing and stacking was not controlled as precisely as achieved in this work. [20,21]. This placement is possible due to the controlled rotation (variable speed and direction) of the mandrel, as opposed to the free spinning, single speed mandrel rotation used in previous methods. This added control enables placement of a fiber such that each length begins precisely in a predetermined location in order to enable the deposition of fibers upon each other to form a layered, repetitive structure. These predetermined locations are the turning points, described here as the pivot points, the point where one length span of the tube is completed and a direction change occurs to move back the other direction.

Using the controlled mandrel in conjunction with the web-based application, a wide variety of tubular frames were produced and characterized, comparing each physical feature to its original programmed counterpart to determine accuracy and reproducibility. The tubes within this study were designed as frames for nerve guides to fit a large-gap peripheral nerve injury model (14–20 mm length; 1.5 mm inner diameter) for the sciatic nerve of a young adult rat [23]. Such tubes have potential in reinforcing hydrogel nerve guides, to prevent their collapse within in vivo applications [24,25]. Mechanical testing was also completed to correlate how variation in winding angle, pore size and number of layers influence the mechanical properties when a tangential compressive force is applied, as would be expected in a nerve guide application [24]. All of the direct-written fibers within the tubes had an average diameter of 18.2 ± 2.1 μm as measured from SEM across all samples printed (n = 32).

3.1. MEWTubes web-based application

The web application was developed to simplify the process of designing tubes and the associated machine code for the MEW printing process. To achieve 3D printed tubes there are five key variables which are required for the machine code; the rotational and translational velocities, the pivot angle, scaffold length and revolution multiplier. All of these variables control the printer's motion, but they are mostly secondary variables calculated using tube design parameters such as winding angle, radius, number of pivot points/pore size. Therefore, the web-application enables users to design a tube based on physical features and the application calculates the required output variables for the machine code, so that the user is not required to work with the mathematical relationship underpinning the fiber path. Table 2 shows how some of these design variables relate to the required output variables which were described in more detail in the Methods section.

The MEWTubes application (found at http://mewtubes.herokuapp.com) presents a user interface with three steps. Firstly, "User Inputs" requires initial values such as the winding angle and radius. In the second step, "User Selection" these initial values are used to compile a list of lengths with an associated number of pivot points and pore sizes, from which the user must select a length. Within this step a second table is also produced listing possible velocity combinations; a user must select an appropriate value for their machine and settings. The third and final step, "Outputs", is the culmination of these parameter selections to depict a graphical representation of the user-designed frame and outputs the required machine code to 3D print this structure on the described tubular MEW printer.

Within these steps there are three major algorithms used within the web-based application. Firstly, the velocity calculations (Eqs. (1.1)–(1.3)). Displayed as a selection list in the "User Selection" step, the chosen values determine the translation and rotation speed of the mandrel and are crucial variables in the output code. The second important mathematical relationship is the equations required to determine discrete length values for a users' tube design. Explained mathematically in the Methods section and shown in Table 2; when the user selects a pivot point/length combination, the application can determine how many mandrel rotations are performed within a length iteration ($F_m + R_m$), the pivot point locations around the mandrel (α), and when the mandrel should change direction (L). While not all of these values are relevant to the user, they are crucial to the machine code (generated in "Outputs") required to accurately fabricate the designed tube.

The final algorithm simulates the digital representation of the tube to be fabricated. The simulated printing path shown in "Outputs" can be considered a conglomeration of helices and a helix is defined using standard parametric equations. These standard helix equations assume a full wavelength of 0–2π, however, for an application with user selected lengths, the fraction and wave multiplier must be included to account for the premature change in direction. Hence, the range becomes $t \in [0, (F_m + R_m) \cdot 2\pi)$. The inclusion of the fraction multiplier also adds complexity to the length variable (y-axis – Eq. (6.1)), as the next length must be adjusted to begin from the point where the previous length ended. While the first length iteration (L_0) can be modelled using standard equations, all proceeding lengths include an integer value for L_i to account for this length-shift. After the first length iteration, a change in direction occurs mid-way through the wavelength, and moves back in the opposite direction while continuing the same wave. To build a complete tubular construct, the parametric equations can be generalized as shown in Eq. (6.1). The structure is built up one length at a time until the required number of lengths are completed in order to return to the initial starting point and thereby complete the first layer.

$$\begin{bmatrix} x \\ y \\ z \end{bmatrix} = \begin{bmatrix} r \cdot \cos(t) \\ (-1)^{L_i} \cdot c \cdot (t - (L_i + L_i \mod 2) \cdot (F_m + R_m) \cdot 2\pi \\ r \cdot \sin(t) \end{bmatrix} \tag{6.1}$$

When adapting the y-dimension for a reduced length (<2π) the interval range t is increased by $(F_m + R_m) \cdot 2\pi$ for each successive length iteration. The $(-1)^{Li}$ accommodates the changes in direction of the construct in cases where y is positive (when L_i is even) and negative (when L_i is odd). The y-shift/offset is handled by the $(L_i + L_i \bmod 2)$ multiplier. These equations are a mathematical representation of the code used by the web-based application to visualize the designed tube.

Table 2
Length selection table. For a tube with a 1.5 mm diameter and a 20° winding angle, there is a fixed pitch length (λ) of 12.94 mm. Under these conditions an array of lengths has been calculated based on the equations shown. For each pivot point condition (yellow) there is a fixed pore size (blue) and an array of length to choose from (green). To fabricate these structures the associated pivot angle must be calculated to enable position control of the mandrel position. This table shows three different length options (R_m = 0–2), but infinite revolutions are available (i.e. R_m = 0…n). The colored columns are those displayed within the web-based application. The orange-highlighted length value is that used to form the helical path in Fig. 2a.

Whole number divisor of 360° (η)	Number of pivot points (N)	Pivot angle (α°)	Fraction Multiplier (F_m)	Pore Size (mm^2)	Length 1 (R_m = 0) (mm)	Length 2 (R_m = 1) (mm)	Length 3 (R_m = 2)... (mm)
η = [1...360]	Must be an even number to complete the pivot point pairs Eq. 4.2	=360/N	=1/η	Eq. 5.3	L=(F_m+R_m)λ		
2	2	180	0.500	30.506	6.47	19.42	32.37
4	4	90	0.250	7.627	3.24	16.18	29.13
3	6	60	0.333	3.390	4.32	17.26	30.21
6	6	60	0.167	3.390	2.16	15.11	28.05
8	8	45	0.125	1.907	1.62	14.57	27.51
5	10	36	0.200	1.220	2.59	15.54	28.48
10	10	36	0.100	1.220	1.29	14.24	27.19

3.2. Tube fabrication using the MEWTube application

Existing approaches for the fabrication of MEW tubular structures use a spindle, or a free spinning mandrel [20,21]. This means that the direction and speed of the rotating mandrel is fixed throughout the spinning process. For the MEW printer used in this study, the mandrel is coupled to a DC motor with an encoder attached to enable digital tracking of the speed and position of the mandrel. Using the information from the encoder, the mandrel can be controlled to change speed and direction during a print. With this added capability, control options are made available which can reduce error in the printing process. When one length iteration of a tube is completed, the mandrel can be rotated precisely to the next location to begin the next length. This ensures that any error due to jet instability is limited to one length iteration. If a change of direction was to continue from the end of the previous length there is no guarantee that this length ended in precisely the correct location and over time an accumulation of error is likely to occur, affecting the accurate positioning required for an AM method. In addition, this method of positioning the mandrel at the end of a length is similar to MEW techniques used on a flat plate collector, where a loop is programmed at the end of a length to minimize the lag of the polymer jet and ensure that a length starts and ends at the correct location [19].

Using the digitally controlled mandrel in conjunction with the web-based application, a large array of tubular frames were printed. Fig. 3, shows the bulk of the samples fabricated for this study. In addition to those displayed in Fig. 3, the 20° range also includes 14, 16 and 18 pivot point samples, while the 30° set also includes 14 pivot point samples. It is important to note that the tubes tested and displayed in Fig. 3 do not represent the full range of parameters achievable with MEW or the MEWTube application. The web-based application can generate machine code for winding angles between as 1° and 89°. Samples with an increased number of pivot points are also possible. Given that the effective velocity can influence the fiber diameter, within this study it was considered essential to maintain this velocity (506 mm/min) for all samples produced, however it became apparent that this effective velocity was not appropriate for the full sample range. Due to this process-based limitation, samples with 60° and 70° winding angles and a higher number of pivot points could not be fabricated reliably. These samples required rapid rotation velocities (as compared to the lower winding angles) and this rotation caused jet instabilities which, in turn, limited the accuracy of fiber deposition. If not limiting the effective velocity to remain constant across a large sample space, it is expected that velocity parameters could be found to achieve reliable printing across a spectrum of winding angle variations.

3.3. Tube characterization

To determine the accuracy and reproducibility of this printing method and the web-based application, the array of tubular frames fabricated (Fig. 3) were characterized and compared against the simulated/designed structures. Initially a visual study of the tubes was conducted to understand the morphology of the produced structures and confirm that they conform to the simulated model presented online.

3.3.1. Morphology

An important morphological observation shown in Fig. 3 relates to the respective pore size and shape. For a fixed winding angle, an increase in pivot points results in an increased fiber density and therefore decreased pore size. With regard to the pore morphology; a 20° winding angle has a diamond shape, with the major axis running parallel to the major axis of the tube. This is similar for a 30° winding angle. However the major axis becomes shorter, thereby resulting in a less elongated diamond shape. At 45° the pore becomes a square with each angle inside the polygon now theoretically equaling 90° and there is no major axis. When moving beyond this center point to tubes with 60° and 70° winding angles, the major axis of the polygon now runs perpendicular to the major axis of the tubes.

The selected number of pivot points for a structure is a discrete, easily identifiable morphological feature of these tubes, for every chosen length (from the web-based application) there are a corresponding number of pivot points. Supplementary Fig. S3 shows the SEM images of a number of printed structures focusing on these pivot point at each end. In every instance, the number of pivot points was found to equal that of the theoretical model. However, as Fig. 4 depicts there was one key difference between the printed models compared to the theoretical. While the simulated structure enables the immediate redirection at the pivot points, the direct-written structure is subject to lag in the polymer

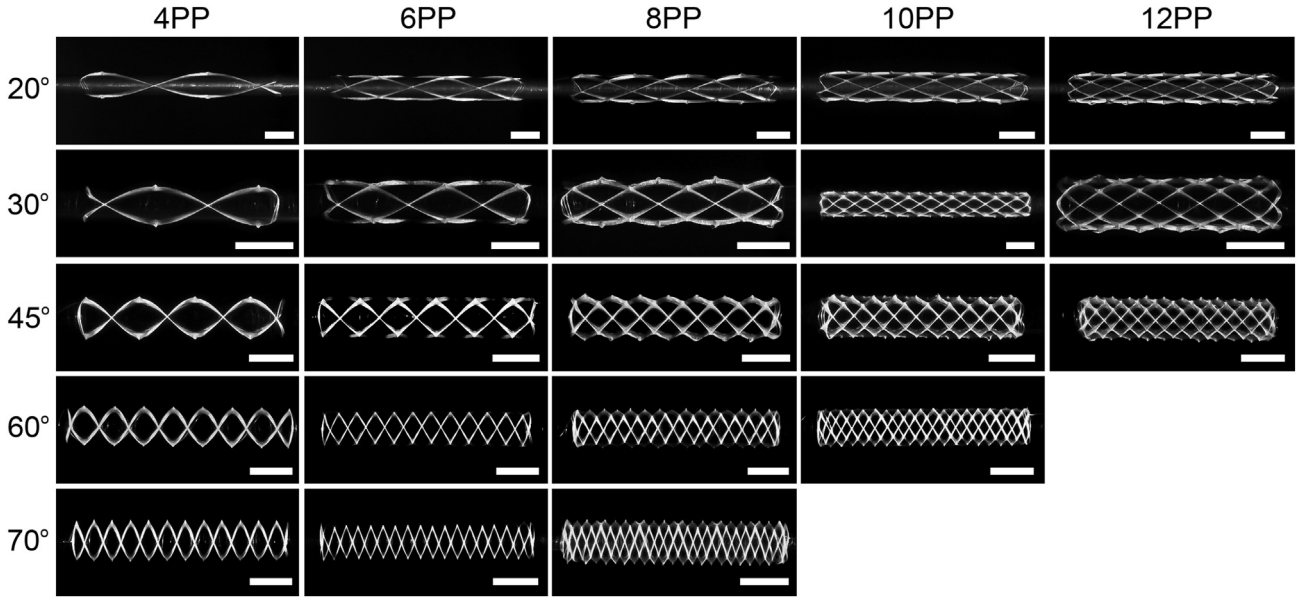

Fig. 3. Dark-field stereomicroscope photos of tubes still on the mandrel collector, showing changes in the number of pivot points (PP) and winding angle. Each of these samples were printed using approximately the same effective velocity (506 mm/min). Given this fixed effective velocity, accurate samples could not be produced for the 70° - 10 PP and 12 PP cases as well as the 60° - 12 PP condition. All scale bars = 2 mm.

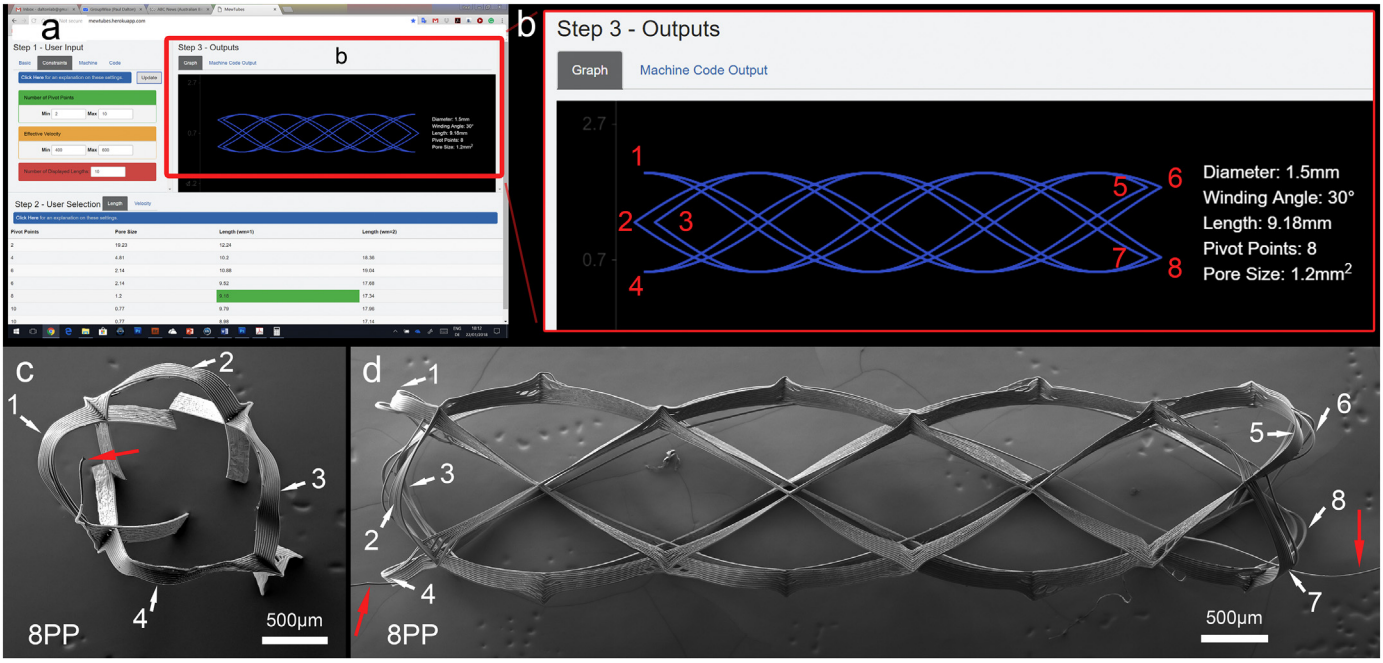

Fig. 4. a) A screenshot of the website showing b) the printing path for an eight pivot point (PP) example tube. SEM images of the fabricated tube from the c) end-view or d) longitudinal view. The pivot points are the part of the frame where the stacked fibers change direction back along the mandrel and mark the end of the tube. The incoming and outgoing fibers are indicated with red arrows.

jet, as well as the rate of mandrel rotation and position change. Therefore, the SEM images of printed models (Fig. 4b, c) have rounded pivot points as compared to the sharp instantaneous points seen in the graphical modelled simulations (Fig. 4a). These same influences are what cause the unordered stacking at the structure ends which can be seen in a number of the samples in Supplementary Fig. S3.

Despite some misalignments in the end of the tubes, all samples showed controlled intentional stacking of fibers. Fig. 5 shows in more

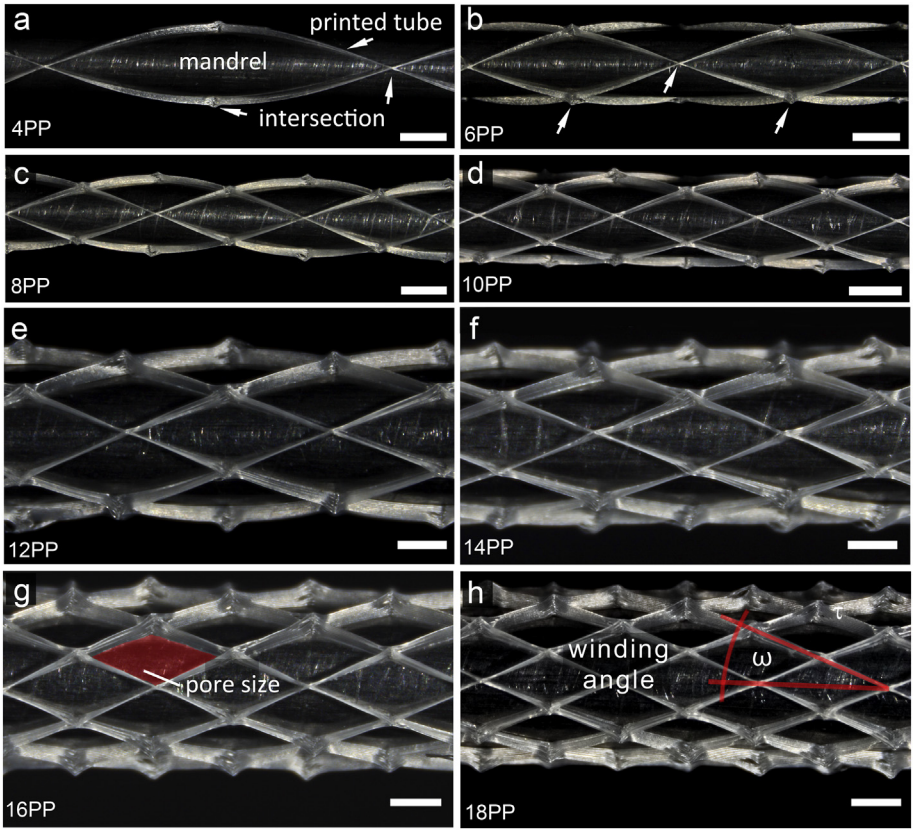

Fig. 5. Photographs of MEW frames on the metal mandrel all with a fixed winding angle of 20°, with a decreasing pore size resulting from an increase in the pivot points (PP). An example of the pore size measurement area and winding angle measurement is indicated in (g) and (h) respectively. The scale bars are 1 mm (a–d) and 0.5 mm (e–h).

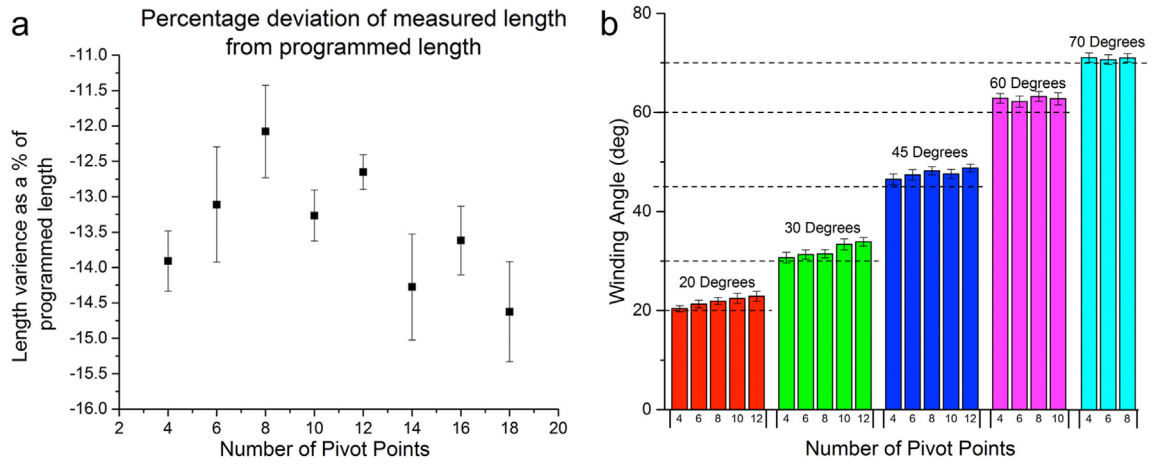

Fig. 6. a) Graph showing the difference in the measured and programmed length as a percentage of the original programmed length – which varies for each pivot point condition. All samples within this graph have a 20° winding angle with standard deviation (n = 15) shown. b) The measured winding angles for the sample set shown in Fig. 3. Each column is an averaged value (n = 30) with the standard deviation indicated.

detail a spectrum of samples printed with a 20° winding angle and varying pivot points. Across this range, it can be observed that there is deliberate and obvious control over fiber spacing, stacking and winding angle, all with the precise fiber deposition expected from an AM technique. For a fixed number of pivot points and increased winding angle, the pore size also decreases (Fig. 5).

3.3.2. Length

It was expected that the printed length would differ from the programmed length due to a lag in the polymer jet [19] with the magnitude of error being affected by the speed of the axes. One challenge for MEW is to accurately place fibers at the ends of the tube where changes in the direct-writing direction are at their maximum, and the jet shape impacts placement. Since the nozzle for MEW is not in direct contact with the collector, there is a lag of the electrified jet (Fig. 1a), which can have fundamental implications for the control of printing particularly when there is a change in writing direction. Hence in this study, the poorest resolution of the print was the planned length. Ideally, no lag will exist if the speed of the axes is set to the same speed as the electrified jet, defined as the critical translation speed (CTS). In practice, due to slight fiber pulsing [19], it is challenging to achieve stable printing with no lag in the polymer jet. To validate the printed lengths the difference between the programmed and measured length was quantified and shown as a percentage of the programmed length in Fig. 6a. The variance percentage fluctuates across each printing condition but is always negative, reflecting the measured length being less than the programmed length. It should be noted that while these tubes were made over the period of one week, the high-voltage, pressure, temperature and all other machine configuration parameters were held constant, suggesting environmental factors influenced jet stability and therefore the printed length accuracy. The average length reduction between the designed length and printed length across all measured conditions was calculated to be −1.95 mm ± 0.18 mm or −13.44% ± 0.55%. The data in Fig. 6a is comprised of the lengths measured from the 20° sample set 4–18 pivot points (n = 15).

3.3.3. Winding angle

The winding angle is one of the most versatile parameters that impacts the overall mechanical properties of a fibrous tube, and is therefore important to control when mimicking the properties of biological tubular structures [26]. The ability to accurately control the winding angle is one of the key parameters that distinguishes this method from solution electrospinning of tubes [27], and allows working as part of other manufacturing concepts, such as 4D printing [28]. Therefore, it was important that this variable could be reproduced as per the required design.

Supplementary Fig. S4 demonstrates how the printed length of a tube can affect the winding angle accuracy. When the mathematics is

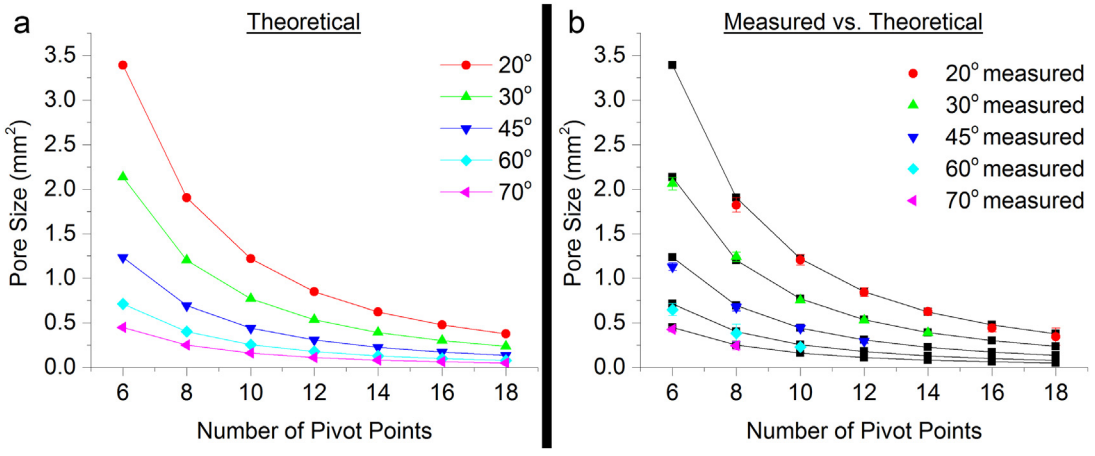

Fig. 7. A comparison between the theoretical and measured pore sizes with respect to number of pivot points (PP) in the tube. The theoretical measurements of each winding angle condition are shown (a) while (b) shows the theoretical values (black points) compared to the measured (colored points) pore size for each winding angle condition.

Table 3
Tube weights and parameters for mechanically tested sample sets.

Number of pivot points (PP)	Theoretical pore size (mm^2)	Average weight (mg)	Programmed length (mm)	Weight/mm of tube (mg)	Number of rotations within a length (R_m)
Group 1: 45° winding angle; 10 layers					
6 PP	1.23	0.28 ± 0.02	10.2	0.03	2
8 PP	0.70	0.40 ± 0.02	10.01	0.04	2
10 PP	0.44	0.50 ± 0.02	9.89	0.05	2
12 PP	0.31	0.58 ± 0.03	9.82	0.06	2
Group 2: 45° winding angle; 80 iterations					
6 PP	1.23	0.42 ± 0.02	10.2	0.04	2
8 PP	0.70	0.36 ± 0.02	10.01	0.04	2
10 PP	0.44	0.37 ± 0.03	9.89	0.04	2
12 PP	0.31	0.37 ± 0.01	9.82	0.04	2
Group 3: angle comparison; fixed pore size					
20°; 16PP	0.47	0.36 ± 0.02	13.75	0.03	1
30°; 14PP	0.40	0.28 ± 0.02	8.75	0.03	1
45°; 10PP	0.44	0.36 ± 0.02	9.89	0.04	2
60°; 8PP	0.40	0.53 ± 0.02	11.22	0.05	4
70°; 6PP	0.45	0.71 ± 0.02	10.86	0.07	6

considered it shows us that the length is dependent on the pitch length of the helix, which is dependent on the winding angle. If the length is stretched or compressed away from the calculated/programmed value, the pitch length is as well, which in turn moves the winding angle away from its intended value. If a larger length is used, the resultant winding angle becomes smaller to compensate and conversely, the use of a small length results in a larger winding angle. These results show that the length directly influences the winding angle and that perfect winding angle reproduction cannot occur unless the length is also accurately produced.

While Fig. 6a showed that the printed length was affected by the accuracy of the jet lag, Fig. 6b shows that the winding angle is also affected, albeit minimally. For the total sample set, with 66 individual tubes and 660 measurements taken, the measured angle was on

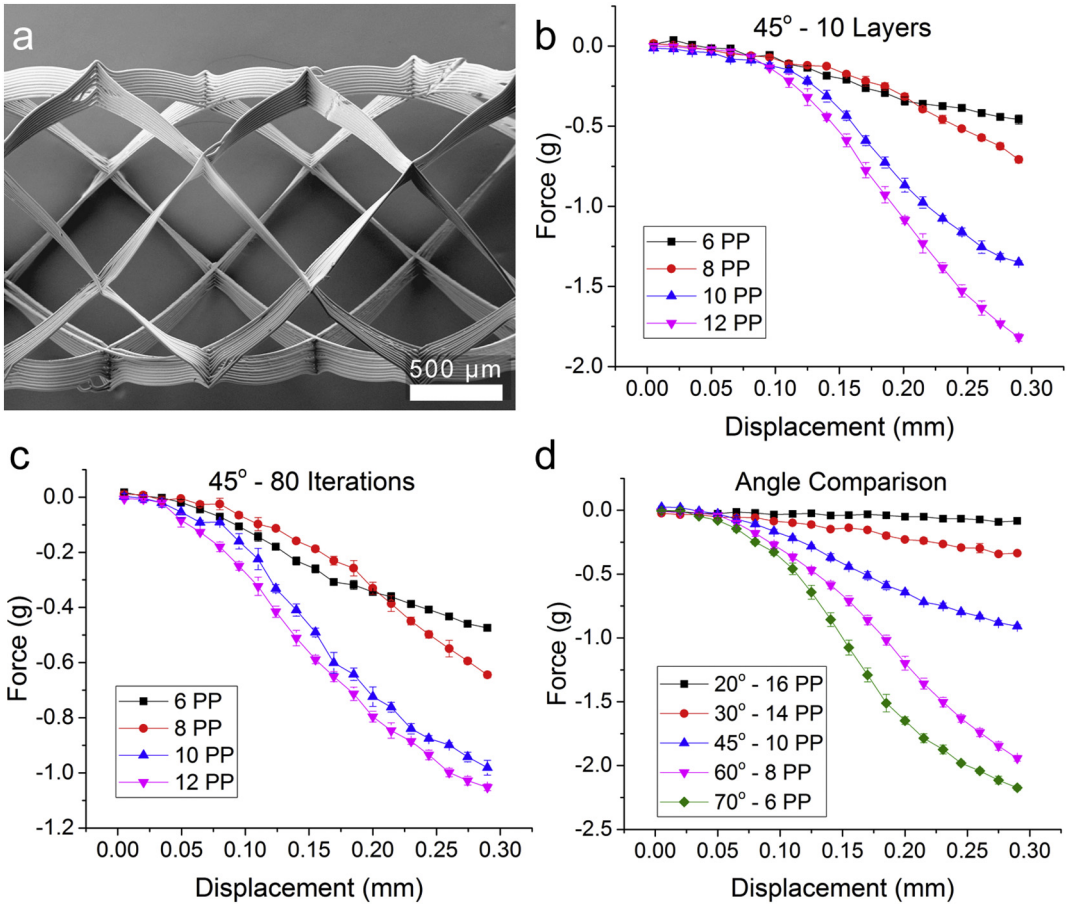

Fig. 8. Mechanical testing of various tubes. A) SEM image of a tube made with winding angle 45°, with 8 pivot points (PP) and 10 layers. Compression forces on tubes with 45° winding angle and various pivot points as B) 10 layers or C) 80 iterations. D) Shows the compressive forces on tubes of various winding angles and pivot points, maintaining the pore size between 0.40 and 0.47 mm^2.

average 2.2° ± 0.9° greater than the designed value. This increase in angle can be attributed to the known length reduction. A decrease in the length due to the jet lag has resulted in an increase in the winding angle for every condition captured, a result corroborating the data found in Supplementary Fig. S4. Across each of the winding angle sets, there is no clear relationship indicating how the number of pivot points affects the winding angle.

3.3.4. Pore size

The theoretical pore size was calculated for all samples using the winding angle and arc length, as explained in the Methods Section. The results of these calculations can be seen in Fig. 7a. As the number of pivot points increase, the influence of the winding angle on the pore size decreases. In Fig. 7a, there is still a difference between each of the winding angles at the 18 pivot point samples, but the trend appears to asymptote. This shows that the number of pivot points has a greater influence on the fiber density and pore size than the winding angle. However, the winding angle dictates the rate of change; in that a 20° winding angle has a much more significant pore size change as the number of pivot points increases, as compared to the 70° samples. This relationship between pore size, number of pivot points and winding angle was previously depicted experimentally in Fig. 3.

Fig. 7 compares the theoretical pore size against the measured pore size. In all instances, the measured size was extremely close to the theoretical size, with some expected exceptions. The measurement method has limits since a two-dimensional image was used, which doesn't account for the curvature of the mandrel. It is for this reason that no value could be obtained for the 20° six pivot point sample, as the pore wrapped too far around the mandrel. However, in all other winding angle conditions the six pivot point sample had the greatest level of deviation from the theoretical value. It was hypothesized that when the curvature was too great, the measured value would underestimate the actual size. This expectation appears to hold for all instances of six pivot points, where the greatest deviation exists.

3.3.5. Mechanical testing

Tubes with variations in their winding angle, pore size and number of layers were mechanically tested in compression. Since the number of pivot points in a tube affects its overall weight (Table 3; Group 1), two types of tubes were printed. Firstly, a 45° winding angle was deposited and 10 layers were stacked on top of each other, as shown in Fig. 8a, b. The sample with the largest number (12) of pivot points resisted the greatest load, which would be expected as the greater number of pivot points reduces the pores size and increase the fiber density and number of intersections.

To compensate for strength reinforcement through greater total mass, a second group of tubes was printed with 80 length iterations - the number of length spans completed regardless of whether pivot point pairs were completed. Fig. 8c shows that those tubes with an increasing number of pivot points also resisted more compression, even though the mass increase did not occur (Table 3; Group 2). This means that tubes with an increased number of pivot points (with a corresponding reduced pore size) will perform better in compression even when compensating for the increased fiber density.

For the third printing group, the winding angle was changed while maintaining a pore size of approximately 0.4 mm^2 (Fig. 8d). As shown (in Table 3; Group 3), this resulted in a varied number of pivot points for each winding angle condition. In each case, a length value was chosen to be as close to 10 mm as possible. However, to achieve a similarity in length the number of mandrel rotations (R_m) within a single length varies for each condition. Therefore, despite printing each sample with only 80 length iteration in an attempt to equalize the mass, slight weight variation still existed due to the additional winding within a single length iteration.

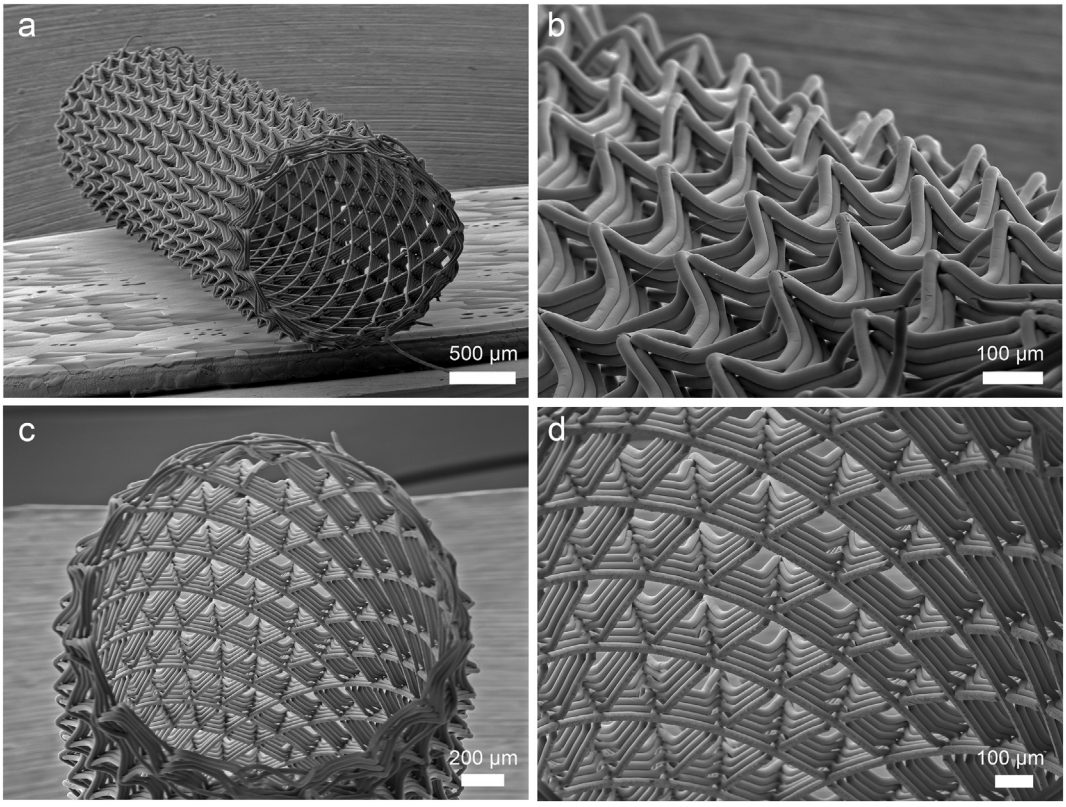

Fig. 9. A 30-pivot point tube, made using a 20° winding angle and designed with the web-based application. a–d) are SEM images of the resultant tube a) showing an overall perspective, b) magnifying the outer surface, where a series of intersecting fibers occur, and c) inside the lumen looking outwards and with d) magnification.

Fig. 8d shows how such tubes resist compression with increasing winding angle and pivot points. While this trend indicates that the larger winding angles resist more compressive force, it should be noted that these samples also have a greater mass of polymer due to the increased number of rotations completed in a single length iteration. It cannot be conclusively stated that the winding angle alone influences the compressive capabilities, however it likely correlates. As Fig. 8b and c show, when the volume of fiber is accounted for, the trend remains. The morphology of the pores and orientation of the major and minor axis theoretically support that 60° and 70° winding angles will resist greater compressive forces.

3.4. Using MEWTubes web-based application for the fabrication of complex tubes

With the ability to accurately control such parameters validated, the web-based software can be used to make a tube with both a low pore size and high number of pivot points. Fig. 9 shows a tube with a winding angle of 20° and 30 pivot points, with an internal diameter of 1.5 mm and wall thickness of approximately 200 μm (Supplementary Fig. S5).

The fabricated tube in Fig. 9 has a series of protrusions on the outer side, due to overlapping fibers doubling the height at the intersections. This is highlighted in Fig. 9b, where a close up micrograph shows this regular, outer, feature. Viewing the tube from end-on, the fibers within the luminal wall are well placed and defined. Fig. 9d shows a magnification of the luminal view, with slight embossing from the mandrel seen on the first fiber deposited. The fiber overlap and sagging that result in the outer protrusions in Fig. 9b can be visualized. Composite SEM images of different samples show the regularity of an entire length of the fabricated tube (Supplementary Fig. S6).

Non-AM approaches for tube manufacture, such as electrospinning [29,30] and melt spinning [22,31–34] have been extensively studied, and indeed put into various applications. The recent discovery of significant reinforcement effects for well-aligned micron-scale MEW fibers embedded within a hydrogel [11,16–18] emphasize the potential of accurate fiber deposition within such soft matter fibrous composites. The approach described here, where a new, open-access, online website is used to plan and generate G-code for MEW printers, allows the design of continuous printing paths onto a cylindrical surface. The deposition accuracy (including with build height) appears to go beyond what is possible for solution electrospinning, even when auxiliary electrodes are used to control fiber placement [35,36].

4. Conclusion

The continuous direct-writing onto a cylinder was approached from a mathematical perspective, and a web-based application, was established to generate the printing path. These results enable a user to select a pivot point/winding angle combination which achieves a pore size closest to their requirements. The measured pore size also matches the theoretical value in almost all instances, further validating the ability of this AM method to fabricate tubular scaffolds as per a designed structure.

The controlled direct-writing onto a cylinder was demonstrated, resulting in defined frames that are distinct to previous MEW structures. A small diameter (1.5 mm) tubular frame was fabricated, to appreciate the strengths and weakness of the MEW process. The PCL tubes fabricated here have applicability themselves as biomaterials, in tubular sites and orifices within the body. In addition, MEW fibers are known to significantly reinforce hydrogels, due to their dimensions and accurate fiber placement. The mathematical approach and software application described here allows such improved fiber placement for tubes made with such electrohydrodynamic jetting methods.

Supplementary data to this article can be found online at https://doi.org/10.1016/j.matdes.2018.05.036.

Data availability

The raw/processed data required to reproduce these findings cannot be shared at this time due to technical or time limitations.

Acknowledgements

The authors appreciate the assistance of Dave Finster for assistance reviewing the code written in this study. The technical assistance of Andrei Hrynevich with SEM is greatly appreciated as well as the support of Niccoló Traverso Ziani for his initial mathematical description of the printing process. We appreciate the EACEA programme BIOFAB (grant# 2013/3137 001-001) that supported Erin McColl, the European Research Council (ERC) (consolidator grant Design2Heal, contract #617989) for their financial support as well as the German Research Foundation (DFG) State Major Instrumentation Programme for funding the Zeiss Crossbeam CB 340 SEM (INST 105022/58-1 FUGG).

References

[1] F.P.W. Melchels, M.A.N. Domingos, T.J. Klein, J. Malda, P.J. Bartolo, D.W. Hutmacher, Additive manufacturing of tissues and organs, Prog. Polym. Sci. 37 (8) (2012) 1079–1104.
[2] N. Guo, M.C. Leu, Additive manufacturing: technology, applications and research needs, Front. Mech. Eng. 8 (3) (2013) 215–243.
[3] A.A. Zadpoor, J. Malda, Additive manufacturing of biomaterials, tissues, and organs, Ann. Biomed. Eng. 45 (1) (2017) 1–11.
[4] L. Leng, A. McAllister, B.Y. Zhang, M. Radisic, A. Gunther, Mosaic hydrogels: one-step formation of multiscale soft materials, Adv. Mater. 24 (27) (2012) 3650–3658.
[5] J. Russias, E. Saiz, S. Deville, K. Gryn, G. Liu, R.K. Nalla, A.P. Tomsia, Fabrication and in vitro characterization of three-dimensional organic/inorganic scaffolds by robocasting, J. Biomed. Mater. Res. A 83((2) (2007) 434–445.
[6] M.A. Skylar-Scott, S. Gunasekaran, J.A. Lewis, Laser-assisted direct ink writing of planar and 3D metal architectures, Proc. Natl. Acad. Sci. 113 (22) (2016) 6137–6142.
[7] H. Tseng, J.A. Gage, W.L. Haisler, S.K. Neeley, T. Shen, C. Hebel, H.G. Barthlow, M. Wagoner, G.R. Souza, A high-throughput in vitro ring assay for vasoactivity using magnetic 3D bioprinting, Sci. Reports 6 (2016), 30640.
[8] P.D. Dalton, Melt electrowriting with additive manufacturing principles, Curr. Opin. Biomed. Eng. 2 (2017) 49–57.
[9] C.B. Dayan, F. Afghah, B.S. Okan, M. Yıldız, Y. Menceloglu, M. Culha, B. Koc, Modeling 3D melt electrospinning writing by response surface methodology, Mater. Des. 148 (2018) 87–95.
[10] A. Hrynevich, B. Sen Elci, J.N. Haigh, R. McMaster, A.B. Youssef, C. Blum, T. Blunk, H.G.J. Groll, D. Dalton Paul, Dimension-based design of melt electrowritten scaffolds, Small (2018), 1800232. https://doi.org/10.1002/smll.201800232.
[11] J. Visser, F.P.W. Melchels, J.E. Jeon, E.M. van Bussel, L.S. Kimpton, H.M. Byrne, W.J.A. Dhert, P.D. Dalton, D.W. Hutmacher, J. Malda, Reinforcement of hydrogels using three-dimensionally printed microfibres, Nat. Commun. 6 (2015) https://doi.org/10.1038/ncomms7933.
[12] B. Delalat, F. Harding, B. Gundsambuu, E.M. De-Juan-Pardo, F.M. Wunner, M.-L. Wille, M. Jasieniak, K.A.L. Malatesta, H.J. Griesser, A. Simula, D.W. Hutmacher, N.H. Voelcker, S.C. Barry, 3D printed lattices as an activation and expansion platform for T cell therapy, Biomaterials 140 (2017) 58–68.
[13] E. Dondossola, B.M. Holzapfel, S. Alexander, S. Filippini, D.W. Hutmacher, P. Friedl, Examination of the foreign body response to biomaterials by nonlinear intravital microscopy, Nat. Biomed. Eng. 1 (2016) 0007.
[14] J.G. Baldwin, F. Wagner, L.C. Martine, B.M. Holzapfel, C. Theodoropoulos, O. Bas, F.M. Savi, C. Werner, E.M. De-Juan-Pardo, D.W. Hutmacher, Periosteum tissue engineering in an orthotopic in vivo platform, Biomaterials 121 (2017) 193–204.
[15] C. Vaquette, S. Ivanovski, S.M. Hamlet, D.W. Hutmacher, Effect of culture conditions and calcium phosphate coating on ectopic bone formation, Biomaterials 34 (22) (2013) 5538–5551.
[16] O. Bas, D. D'Angella, J.G. Baldwin, N.J. Castro, F.M. Wunner, N.T. Saidy, S. Kollmannsberger, A. Reali, E. Rank, E.M. De-Juan-Pardo, D.W. Hutmacher, An integrated design, material, and fabrication platform for engineering biomechanically and biologically functional soft tissues, ACS Appl. Mater. Interfaces 9 (35) (2017) 29430–29437.
[17] M. de Ruijter, A. Hrynevich, J.N. Haigh, G. Hochleitner, M. Castilho, J. Groll, J. Malda, P.D. Dalton, Out-of-plane 3D-printed microfibers improve the shear properties of hydrogel composites, Small 14 (2018) 1702773.
[18] O. Bas, S. Lucarotti, D.D. Angella, N.J. Castro, C. Meinert, F.M. Wunner, E. Rank, G. Vozzi, T.J. Klein, I. Catelas, E.M. De-Juan-Pardo, D.W. Hutmacher, Rational design and fabrication of multiphasic soft network composites for tissue engineering articular cartilage: a numerical model-based approach, Chem. Eng. J. 340 (2018) 15–23.
[19] G. Hochleitner, A. Youssef, A. Hrynevich, J.N. Haigh, T. Jungst, J. Groll, P.D. Dalton, Fibre pulsing during melt electrospinning writing, BioNanoMaterials 17 (3) (2016) 159–171.
[20] T. Jungst, M.L. Muerza-Cascante, T.D. Brown, M. Standfest, D.W. Hutmacher, J. Groll, P.D. Dalton, Melt electrospinning onto cylinders: effects of rotational velocity and collector diameter on morphology of tubular structures, Polym. Int. 64 (9) (2015) 1086–1095.

[21] T.D. Brown, A. Slotosch, L. Thibaudeau, A. Taubenberger, D. Loessner, C. Vaquette, P.D. Dalton, D.W. Hutmacher, Design and fabrication of tubular scaffolds via direct writing in a melt electrospinning mode, Biointerphases 7 (2012)https://doi.org/10.1007/s13758-011-0013-7.
[22] B. Gupta, A.R. Ray Geeta, Preparation of poly(epsilon-caprolactone)/poly(epsilon-caprolactone-co-lactide) (PCL/PLCL) blend filament by melt spinning, J. Appl. Polym. Sci. 123 (4) (2012) 1944–1950.
[23] P.D. Dalton, J. Mey, Neural interactions with materials, Front. Biosci. 14 (2009) 769–795.
[24] J.S. Belkas, C.A. Munro, M.S. Shoichet, M. Johnston, R. Midha, Long-term in vivo biomechanical properties and biocompatibility of poly(2-hydroxyethyl methacrylate-co-methyl methacrylate) nerve conduits, Biomaterials 26 (14) (2005) 1741–1749.
[25] P.D. Dalton, M.S. Shoichet, Creating porous tubes by centrifugal forces for soft tissue application, Biomaterials 22 (19) (2001) 2661–2669.
[26] J. Basu, J.W. Ludlow, Platform technologies for tubular organ regeneration, Trends Biotechnol. 28 (10) (2010) 526–533.
[27] W.E. Teo, M. Kotaki, X.M. Mo, S. Ramakrishna, Porous tubular structures with controlled fibre orientation using a modified electrospinning method, Nanotechnology 16 (6) (2005) 918.
[28] F. Momeni, S.M. Mehdi, N. Hassani, X. Liu, J. Ni, A review of 4D printing, Mater. Des. 122 (2017) 42–79.
[29] T.M. Dinis, R. Elia, G. Vidal, Q. Dermigny, C. Denoeud, D.L. Kaplan, C. Egles, F. Marin, 3D multi-channel bi-functionalized silk electrospun conduits for peripheral nerve regeneration, J. Mech. Behav. Biomed. Mater. 41 (2015) 43–55.
[30] S.R. Son, R.A. Franco, S.H. Bae, Y.K. Min, B.T. Lee, Electrospun PLGA/gelatin fibrous tubes for the application of biodegradable intestinal stent in rat model, J Biomed Mater Res B Appl Biomater 101B (6) (2013) 1095–1105.
[31] Q. Liu, M. Zhao, Y. Zhou, Q. Yang, Y. Shen, R.H. Gong, F. Zhou, Y. Li, B. Deng, Polylactide single-polymer composites with a wide melt-processing window based on core-sheath PLA fibers, Mater. Des. 139 (2018) 36–44.
[32] R. Hufenus, L. Gottardo, A.A. Leal, A. Zemp, K. Heutschi, P. Schuetz, V.R. Meyer, M. Heuberger, Melt-spun polymer fibers with liquid core exhibit enhanced mechanical damping, Mater. Des. 110 (2016) 685–692.
[33] S.W. Chung, N.P. Ingle, G.A. Montero, S.H. Kim, M.W. King, Bioresorbable elastomeric vascular tissue engineering scaffolds via melt spinning and electrospinning, Acta Biomater. 6 (6) (2010) 1958–1967.
[34] J.E. Spruiell, E. Bond, Melt spinning of polypropylene, in: J. Karger-Kocsis (Ed.), Polypropylene: An A–Z Reference, Springer Netherlands, Dordrecht 1999, pp. 427–439.
[35] M.M.L. Arras, C. Grasl, H. Bergmeister, H. Schima, Electrospinning of aligned fibers with adjustable orientation using auxiliary electrodes, Sci. Technol. Adv. Mater. 13 (3) (2012), 035008.
[36] J. Zhao, H. Liu, L. Xu, Preparation and formation mechanism of highly aligned electrospun nanofibers using a modified parallel electrode method, Mater. Des. 90 (2016) 1–6.